Effect of transverse and longitudinal reinforcement ratios on the behaviour of RC T-beams shear-strengthened with embedded FRP bars

Sogut, Kagan; Dirar, Samir; Theofanous, Marios; Faramarzi, Asaad; Nayak, Amar Nath

DOI:
10.1016/j.compstruct.2021.113622

EFFECT OF TRANSVERSE AND LONGITUDINAL REINFORCEMENT RATIOS ON THE BEHAVIOUR OF RC T-BEAMS SHEAR-STRENGTHENED WITH EMBEDDED FRP BARS

Kagan Sogut[a*], Samir Dirar[b], Marios Theofanous[c], Asaad Faramarzi[b] and Amar Nath Nayak[d]

[a]PhD Researcher, University of Birmingham, Edgbaston, Birmingham, B15 2TT, United Kingdom

[b]Associate Professor, University of Birmingham, Edgbaston, Birmingham, B15 2TT, United Kingdom

[c]Assistant Professor, University of Birmingham, Edgbaston, Birmingham, B15 2TT, United Kingdom

[d]Professor, Veer Surendra Sai University of Technology, Burla-768 018, Odisha, India

*Corresponding author, Email: kxs696@bham.ac.uk

Abstract

Seven reinforced concrete (RC) T-beams, comprising two unstrengthened (control) beams and five beams strengthened in shear with embedded FRP bars, were tested to failure. The test parameters were steel-to-FRP shear reinforcement ratio and tension reinforcement ratio. A nonlinear finite element (FE) model was developed, validated and used to conduct parametric studies. The experimental and FE results showed that the concrete and FRP contributions to shear resistance as well as the total shear force capacity all decrease with increasing steel-to-FRP shear reinforcement ratio. The tension reinforcement ratio influenced the failure mode of the tested and modelled beams but had insignificant impact on shear strength enhancement. The experimental results were compared with the FE and Concrete Society Technical Report 55 predictions. The FE model correctly reproduced the experimental results and gave accurate predictions, with a mean predicted-to-experimental ratio of 1.04, whereas TR55 gave conservative predictions, with a mean predicted-to-experimental ratio of 0.42.

Keywords: beam; concrete; embedded bars; fibre reinforced polymer; finite element; shear; strengthening

1. Introduction

Heavier traffic loads, poor initial design, aggressive exposure conditions, natural or man-made extreme events and steel reinforcement corrosion can all deteriorate the shear strength of existing reinforced concrete (RC) structures [1]. Many cost-effective, practical and durable fibre reinforced polymer (FRP) shear strengthening solutions have emerged in response to the increasing number of shear-deficient concrete structures. For example, externally bonded (EB) [2] and near-surface mounted (NSM) [3] FRP strengthening techniques have been verified to enhance the shear strength of existing RC beams. However, EB and NSM FRP shear strengthening systems require laborious surface preparation and, unless properly anchored, debond prematurely from the concrete. The Deep Embedment (DE) [4], also known as the embedded through-section (ETS) [5], shear strengthening technique used in this study consists of glass FRP (GFRP) or carbon FRP (CFRP) bars embedded into the concrete core to act as additional shear reinforcement. The FRP bars are inserted into epoxy-filled holes drilled throughout the entire depth of the beam, thereby connecting the compression chord to the tension chord and ensuring that truss action can be fully developed. It is acknowledged that it can be difficult to drill holes in members with congested internal steel reinforcement. However, exiting concrete members requiring shear strengthening usually include relatively low amounts of steel reinforcement. The locations of existing steel bars can be obtained from as-built drawings and/or by using cover metres. Besides, core drilling machines with steel bar sensing function can be used to drill holes. Such drilling machines automatically shut off when they touch a steel bar, thereby ensuring integrity of the steel bars.

Previous research work on DE FRP shear strengthening provided valuable findings, particularly with regard to the effects of the presence of internal steel shear reinforcement [6]. An installation technique that does not require access to the top surface of the beam was also developed [4, 5, 7]. The effects of the DE bar diameter and spacing [8], shear link corrosion level [9], shear span-to-effective depth ratio [10] and moment-shear interaction [11] were examined. Analytical models for predicting the contribution of the DE bars to the shear strength were also proposed [6, 8, 12]. However, the effects of other parameters that may also influence the strengthened behaviour have not yet been fully understood. It has been recognised that steel-to-FRP shear reinforcement ratio is one of the main parameters governing the strengthened behaviour. However, experimental and numerical research [e.g. 7, 13]. examining the effect of steel-to-FRP shear reinforcement ratio is limited. Similarly, tension reinforcement ratio has been demonstrated to influence the behaviour of EB FRP-strengthened beams [2]. However, the effect of tension reinforcement ratio on the behaviour of DE FRP-strengthened beams has not yet been identified.

Using physical tests and nonlinear finite element (FE) modelling, this paper critically investigates the effect of steel-to-FRP shear reinforcement ratio and tension reinforcement ratio on the behaviour of RC T-beams strengthened in shear with DE FRP bars. The experimental and FE results are used to assess the accuracy of the Concrete Society's Technical Report 55 (TR55) [14] design model for DE FRP shear strengthening.

2. Research Significance

Shear strengthening of existing RC structures with embedded FRP bars is an area with great potential, particularly in situations when the flange and/or web are inaccessible. The embedded FRP bars are less susceptible to debonding issues when compared with unanchored EB and NSM shear strengthening systems. Yet, the effect of transverse and longitudinal reinforcement ratios is not fully understood. This study provides valuable insights into the effect of these two parameters on the strengthened behaviour. Moreover, it identifies limitations in current shear strengthening design guidance and presents an accurate predictive tool that has been demonstrated to be an improvement over existing design practice.

3. Experimental Programme

3.1. Specimens

The experimental programme consisted of two unstrengthened (control) and five DE FRP-strengthened RC T-beams. The unstrengthened beams had a two-part designation whereas the strengthened beams had a three-part designation. The first part indicates that a beam was either a control (C) or a strengthened (S) specimen. The second part denotes the percentage of tension reinforcement (either 2.0 or 2.7) in the maximum moment zone. The percentage of tension reinforcement is defined as (100% A_s/b_wd) where A_s is the area of tension reinforcement, b_w is the web width and d is the effective depth. The third part refers to the type (either glass (G) or carbon (C)) of DE FRP bars and the steel-to-FRP shear reinforcement ratio. The steel-to-FRP shear reinforcement ratio is defined as $(E_sA_{sw}/ b_ws)/(E_fA_f/ b_ws_f)$ where E_s and E_f are the elastic moduli of steel and FRP, respectively; A_{sw} and A_f are the areas of steel and FRP shear reinforcement, respectively; and s and s_f are the spacing of steel and FRP shear reinforcement, respectively. Hence, the designation S/2.7/C1.35 refers to a strengthened beam with a tension reinforcement ratio of 2.7% and steel-to-CFRP shear reinforcement ratio of 1.35.

As can be seen in Fig. 1, the RC T-beams had a flange width of 200 mm, flange depth of about 63 mm, web width of 75 mm and overall height of 325 mm. All beams had an effective depth and a shear span-to-effective depth ratio of about 300 mm and 3.0, respectively. The beams were longitudinally reinforced in compression with one layer of two 8 mm diameter steel bars. The tension reinforcement comprised either four 12 mm diameter steel bars or four 12 mm and two 10 mm diameter steel bars (see Fig. 1), resulting in a tension reinforcement ratio in the maximum moment zone of either 2.0 or 2.7%, respectively. The steel shear reinforcement consisted of 4 mm diameter shear links spaced at 300 mm centre-to-centre (c/c), resulting in a steel shear reinforcement ratio (A_{sw}/ b_ws) of 0.11%. This reinforcement arrangement is representative of earlier design practice in the UK [9]. The DE shear strengthening system consisted of 6 mm diameter sand-coated FRP bars spaced as shown in Fig. 2. The beams with 3 DE bars had an FRP shear reinforcement ratio (A_f/ $b_w s_f$) of 0.125% whereas the beams with 6 DE bars had an FRP shear reinforcement ratio of 0.25%.

3.2. Material Properties

Each RC T-beam was cast from a single batch of ready-mixed concrete with a maximum aggregate size of 10 mm. The concrete mixture proportions were cement: water: sand: coarse aggregate = 1: 0.42: 1.30: 2.65. A superplasticiser (Alphaflow 420) dosage of 0.75% by weight of cement was added to ensure adequate workability of the concrete mix. Standard compression tests were conducted on the day of beam testing on 100 mm cube and 100 mm diameter × 200 mm long cylinder specimens. The results showed that the concrete had average cylinder and cube compressive strength values of 41 and 49 MPa, and standard deviation values of 1.82 and 1.94 MPa, respectively.

The mechanical properties of the steel and DE FRP reinforcement, as declared by the manufacturer, are reported in Table 1. A commercially available high viscosity epoxy resin was used to bond the FRP bars to the concrete. The bond strength, compressive strength, compressive modulus, tensile strength and elongation at failure of the epoxy resin were 12.4 MPa, 82.7 MPa, 1493 MPa, 43.5 MPa and 2%, respectively, as certified by the manufacturer.

3.3. Strengthening Procedure

To install the FRP bars, 9 mm diameter vertical holes were formed in the shear spans of the beams, through the centreline of the cross-section, at the FRP bar locations shown in Fig. 2. The vertical holes were created by installing PVC rods at the required positions within the steel reinforcement cage before casting the concrete. The PVC rods were removed from the concrete 24 hours after casting. A 10 mm diameter drill bit was then used to enlarge the cast-in-place holes. Prior to installing the FRP bars, the drilled holes were roughened by a wire brush and cleaned with compressed air. The lower ends of the holes were sealed and the epoxy resin was used to fill two-thirds of the holes. The FRP bars were covered with a thin layer of the adhesive and inserted into the holes. Any excess epoxy was removed. Many research studies [e.g. 4, 5, 7] have already demonstrated that it is possible to install FRP bars by drilling vertical or inclined holes rather than by using cast-in-place holes. The installation procedure explained above was used for simplicity.

3.4. Test Setup and Instrumentation

The RC T-beams were tested in a three-point bending configuration as shown in Fig. 1. This setup allowed two tests to be conducted on one beam by testing one beam end zone while keeping the other end unstressed and vice versa. The load was applied monotonically using a 1000 kN hydraulic cylinder and measured by a 1000 kN load cell. The vertical deflection under applied load was measured by displacement transducers. The strain in the tension reinforcement at the position of the maximum bending moment was measured using 6 mm strain gauges. The strain in the steel and FRP shear reinforcement was measured using 3 mm strain gauges positioned along the line joining the support and loading point (see Fig. 2). The readings of the 1000 kN load cell, displacement transducers and strain gauges were obtained using a data logger connected to a personal computer.

4. Test Results and Discussion

4.1. Shear Strength

Table 2 gives the unstrengthened shear force capacity, shear force at failure, gain in shear resistance due to the DE FRP bars, and failure mode of each beam.

The control beams (C/2.0 and C/2.7) had a shear strength of about 65.5 and 75.5 kN, respectively. The higher shear strength of C/2.7 is attributable to the higher tension reinforcement ratio, which enhanced dowel action. The tension reinforcement ratio also influenced the failure mode of the strengthened beams. S/2.0/G1.91 failed in flexure whereas S/2.7/G1.91 failed in shear. However, the increase in tension reinforcement ratio from 2.0 to 2.7% had insignificant effect on the gain due to DE GFRP bars. S/2.0/G1.91 and S/2.7/G1.91 had a comparable strength gain of 13 and 15 kN, respectively, whereas the strength gain in both S/2.0/G3.82 and S/2.7/G3.82 was negligible.

The steel-to-FRP shear reinforcement ratio had a clear effect on the shear strength gain. As stated above, the shear strength gain was negligible at a steel-to-FRP shear reinforcement ratio of 3.82. The decrease in steel-to-FRP shear reinforcement ratio from 3.82 to 1.91, through the provision of additional GFRP bars, resulted in a shear strength gain of about 19.8% (13-15 kN) in both S/2.0/G1.91 and S/2.7/G1.91. The further decrease in steel-to-FRP shear reinforcement ratio from 1.91 to 1.35, by using CFRP bars, increased the shear strength gain from 19.8% to 37.2% (28.1 kN). Due to the higher elastic modulus of steel (200 GPa) compared with that of CFRP (130 GPa) or GFRP (46 GPa), steel shear links attract higher forces than DE FRP bars. A low steel-to-FRP shear reinforcement ratio, attainable via a high FRP axial stiffness (E_fA_f) and/or low FRP spacing, is therefore required to achieve significant shear strength enhancement in existing RC structures.

4.2. Deflection Response

Fig. 3 compares the shear force-deflection curves of the tested beams. Except for S/2.0/G1.91, all beams featured a quasi-linear shear force-deflection response up to peak shear force. S/2.0/G1.91 had a ductile failure featuring an approximately 60 mm long plateau. The remaining beams had a brittle shear failure with a sudden drop in load at peak shear force.

All beams had comparable elastic (i.e. uncracked) stiffness. The cracked stiffness of all beams was also comparable up to the formation of inclined cracks at a shear force of about 25 kN. After the formation of inclined cracks, the unstrengthened (control) and GFRP-strengthened beams had comparable cracked stiffness whereas the CFRP-strengthened beam had a stiffer response. The axial stiffness of a CFRP bar (3674 kN per bar) is 2.83 times higher than that of a GFRP bar (1300 kN per bar). The CFRP bars are therefore more effective in resisting inclined crack opening and controlling deflection.

4.3. Cracking and Failure Mode

The crack patterns at failure of the tested beams are depicted in Fig. 4. Except for S/2.0/G1.91, all beams had comparable cracking behaviour. The formation of flexural cracks at the soffit of the beams under the load started at a shear force of about 10 kN. With increased loading, the flexural cracks extended into the shear span. The outermost flexural crack in the shear span turned into an inclined crack at a shear force of about 25 kN. Upon further loading, more inclined cracks appeared in the shear span and, eventually, an inclined crack instigated a diagonal tension failure. Of note is that the inclination of shear cracks at failure increased with decreasing the spacing of the DE GFRP bars. It is well known that decreasing the spacing of transverse reinforcement in a RC beam results in steeper cracks [7, 15]. Moreover, C/2.7/C1.35 had less inclined cracks than C/2.7/G3.82, although both beams were strengthened with 3 DE bars. This can be attributed to the higher elastic modulus of CFRP bars as explained in the preceding section.

The cracking behaviour of S/2.0/G1.91 was comparable to that of the remaining beams up to a shear force of about 60 kN. Upon further loading, the inclined cracks became stable whereas the flexural cracks in the maximum moment zone started to propagate. Eventually, failure took place due to crushing of the concrete adjacent to the loading point.

4.4. Components of Shear Resistance

Strain gauge readings were used to calculate the contributions of the steel and FRP shear reinforcement to the shear force capacity (see Fig. 5). All steel shear links attained or exceeded the yield strain of 0.0027. As the shear crack that caused failure always intersected the steel shear links, the steel contribution (V_s) to shear resistance was calculated as the yield strength of the shear links (540 MPa) multiplied by the cross-sectional area of the two shear links (50.2 mm^2). The FRP contribution (V_f) to shear resistance was based on the strain in the DE FRP bars intersected by the main shear crack that caused failure. The strain in these bars was multiplied by the axial stiffness (E_fA_f) of the FRP bars. For example, V_f in S/2.7/G1.91 was calculated based on the strain in the DE FRP bars G3, G4, G5 and G6 whereas the strain in G1 and G2 was ignored because these two bars were not intersected by the main shear crack. The concrete contribution (V_c) was calculated as the total shear force capacity minus the sum of V_s and V_f.

Fig. 5 presents the components of shear resistance versus shear force for the beams that failed in shear. The steel shear links were inactive up to the formation of inclined cracks and the shear force was resisted by concrete only. After the formation of inclined cracks, the concrete contribution started to diminish with increased loading. Before yielding, the shear links in the strengthened beams resisted lesser shear force than those in the corresponding control beam. This is attributable to the presence of the DE FRP bars, which resisted crack opening and thus reduced the forces in the shear links. Similar to the steel shear links, the DE FRP bars were inactive up to the formation of inclined cracks. However, the DE FRP bars started to contribute significantly to shear resistance only after the yield of the steel shear links. There were no signs of FRP bar debonding up to peak shear force in all tested beams.

An important implication of the results shown in Fig. 5 is that the subtraction of the unstrengthened shear force capacity from the strengthened shear force capacity does not always give a correct estimate of V_f. The overall shear strength gain for S/2.0/G3.82 and S/2.7/G3.82 was negligible (see Table 2). Yet, the strain-based V_f values for these two beams were 28.6 and 32.3 kN, respectively. Similarly, the overall shear strength gain for S/2.7/G1.91 and S/2.7/C1.35 was 15 and 28.1 kN, respectively, whereas the strain-based V_f values were 53.9 and 41.6 kN, respectively. This discrepancy occurs because V_c in the strengthened beams reduces with increased loading. The shear strength gain reported in Table 2 is therefore the difference between the strain-based V_f values and the reduction in V_c values (compared with the corresponding control beam). For example, the shear strength gain for S/2.0/G3.82 is 28.6 kN – (38.4 kN – 13.0 kN) = 3.2 kN.

Figs. 6(a) and 6(b) show the experimental variations in V_c and V_f, respectively, with steel-to-FRP shear reinforcement ratio. The concrete contribution decreased from 34.9 to 9.3 kN with increasing the steel-to-FRP shear reinforcement ratio from 1.35 to 3.82. The relatively higher axial stiffness of the CFRP bars (3674 kN per bar) in S/2.7/C1.35 controlled crack opening and resulted in a relatively high V_c value (34.9 kN). On the other hand, the GFRP bars in the remaining 3 beams that failed in shear were much less effective in controlling crack width and maintaining aggregate interlock. As a result, the GFRP-strengthened beams had relatively low V_c values that varied from 9.3 to 13.0 kN.

The FRP contributions for S/2.7/C1.35 and S/2.7/G1.91 were 41.6 and 53.9 kN, respectively. These values are significantly higher than the corresponding values of 32.3 and 28.6 kN obtained for S/2.7/G3.82 and S/2.0/G3.82, respectively. This result shows that the FRP contribution also decreases with increasing steel-to-FRP shear reinforcement ratio. As explained earlier, this is due to the higher elastic modulus of steel, which resulted in the steel shear links attracting higher forces than the DE FRP bars. Given its implication for the shear strength enhancement, the influence of steel-to-FRP shear reinforcement ratio is further investigated numerically.

5. Finite Element Modelling

A two-dimensional nonlinear FE model was developed using VecTor2 software package. VecTor2 is based on the Disturbed Stress Field Model (DSFM) [16], an extension of the Modified Compression Field Theory (MCFT) [17]. It utilizes a rotating smeared-crack approach to predict the structural behaviour of RC membrane elements. Further details on VecTor2 can be found elsewhere [18].

5.1. Mesh and Element Details

Two-dimensional four-node rectangular plane stress elements with two degrees of freedom at each node were used for the concrete. The concrete mesh size in each direction was taken as $2.5d_a$ (where d_a is the maximum aggregate size). This is broadly consistent with the recommendation of Bažant and Oh [19] to use a concrete mesh size of $3d_a$. Moreover, Dirar et al. [20] successfully used a mesh size of $2.5d_a$ to model FRP shear-strengthened RC T-beams comparable to those reported in this paper. For convenience, the loading and support steel plates had the same element type and size as the concrete.

The steel bars were modelled as discrete reinforcement using two-node truss elements with two degrees of freedom at each node. Bond failure between the concrete and the steel bars was not the governing failure mode of the tested beams. Perfect bond was therefore assumed between the concrete and the steel reinforcement. A similar approach was successfully used by Qapo et al. [13] to model RC T-beams strengthened in shear with DE FRP bars. There is still the potential for localized slip between the reinforcement and surrounding concrete in the tested beams. However, this does not affect the overall predicted behaviour as demonstrated by the comparison between the experimental and numerical results (see *FE Model Validation* section).

The DE FRP bars were modelled using two-node truss elements. Two-node interface elements were used to link the truss elements representing the DE FRP bars to the plane stress elements representing the concrete. This allowed the bond behaviour between the DE FRP bars and surrounding concrete to be modelled.

5.2. Material Modelling

The concrete in compression was modelled by Thorenfeldt's et al. [21] stress-strain curve, which is given by:

$$f_{ci} = -\left(\frac{\varepsilon_{ci}}{\varepsilon_p}\right) f_p \frac{n}{n-1+(\frac{\varepsilon_{ci}}{\varepsilon_p})^{nk}} \tag{1}$$

where f_{ci} (MPa) represents the concrete compressive stress at a given strain ε_{ci} (mm/mm); f_p (MPa) is the concrete cylinder compressive strength and ε_p (mm/mm) is the corresponding strain; n is a parameter equal to 0.8 + (f_p/17) and k, taken as 0.67 + (f_p/62), is a parameter governing the descending branch of Eq. (1). The softening of concrete in compression caused by lateral cracking was incorporated by adopting the model developed by Vecchio and Collins [22]. Poisson's ratio of concrete was taken as 0.15 based on the recommendation of CEB-FIB Model Code 1990 [23].

The concrete behaviour in tension was assumed linear-elastic prior to concrete cracking. A bilinear tension softening model [23] was used to model the post-cracking behaviour of concrete. The fracture energy (G_F) of concrete was calculated according to Eq. 2, also given by CEB-FIB Model Code 1990 [23].

$$G_F = G_{Fo}\left(\frac{f_{cm}}{f_{cmo}}\right)^{0.7} \ (N/mm) \tag{2}$$

where G_{Fo} is the base value of fracture energy (taken as 0.026 N/mm for a maximum aggregate size of 10 mm); f_{cm} is the concrete compressive strength (MPa) and f_{cmo} is equal to 10 MPa. Bentz's model [24] was used to simulate tension stiffening.

An explicit model for shear transfer in cracked concrete was not required because, in the rotating crack model, crack direction changes with the change in direction of the principal tensile stress. It follows that any crack plane in the rotating crack model is a principal plane with no shear stress.

The stress-strain model for the steel reinforcement as well as the loading and support plates had an initial linear-elastic response followed by a yield plateau and a nonlinear strain-hardening phase up to rupture. For the DE FRP bars, a linear-brittle stress-strain model, based on the ultimate strength values reported in Table 1, was used.

The bond-slip results reported by Valerio et al. [6] were used to represent the FRP-to-concrete bond behaviour. These results were selected because they were based on the same epoxy adhesive type as that used in this study. The considered bond-slip tests were carried out on 7.5 mm diameter FRP bars, which are slightly larger than the 6 mm diameter FRP bars used in the tested beams. However, this had insignificant implications for the modelled behaviour (see *FE Model Validation* section).

5.3. Solution algorithm

VecTor2 utilizes an incremental-iterative algorithm to solve the nonlinear equations. A displacement control approach was used where the load was applied in increments of 0.1 mm. For each increment, the secant stiffness was used to iteratively search for equilibrium. Convergence was successfully achieved at the end of each increment using this procedure.

6. FE Results and Discussion

6.1. FE Model Validation

The FE predictions in terms of shear force at failure and deflection at peak load together with the corresponding experimental results are presented in Table 3. The FE predictions were in good agreement with the experimental results. The mean value of the predicted-to-experimental shear force at failure is 1.01 with a standard deviation of 0.07, demonstrating the accuracy of the FE model. The corresponding values for the deflection at peak shear force, excluding S/2.0/G1.91 which failed in flexure, were 0.97 and 0.10, respectively.

Fig. 7 shows that the FE model successfully predicted the overall deflection response of the tested beams. Similar to the experimental results, the predicted shear force-deflection curves were quasilinear prior to cracking. The pre-cracking stiffness was accurately predicted, indicating that the boundary conditions and elastic constants were well modelled. Subsequently, the shear force-deflection curves turned nonlinear due to stiffness deterioration caused by cracking. Upon further loading, the post-cracked stiffness continued to deteriorate up to failure. The ductile failure of S/2.0/G1.91, characterised by a plateau at peak load, as well as the brittle failure of the remaining six beams, characterised by a sudden drop in load, were accurately predicted.

Following the successful validation of the FE model, it was used to obtain further insight into the effect of test parameters on the strengthened behaviour.

6.2. Effect of Steel-to-FRP Shear Reinforcement Ratio

Making use of the validated FE model, a parametric study was conducted to further examine the interaction between DE FRP bars and existing steel shear links. The beams considered in the parametric study were nominally identical to the tested beams but had steel-to-FRP shear reinforcement ratios in the range from 0.17 to 4.35, obtained by changing the diameter and spacing of existing steel shear links and/or the dimeter, spacing and type of DE FRP bar. All modelled beams failed in shear after yielding of the existing steel shear links.

Fig. 8 shows that the variation of steel-to-FRP shear resistance ratio (V_s/V_f) with steel-to-FRP shear reinforcement ratio is bilinear. The DE FRP contribution far exceeds the steel contribution, resulting in V_s/V_f values in the range from 0.08 to 0.22, for steel-to-FRP shear reinforcement ratios in the range from 0.17 to 0.78. With increasing the steel-to-FRP shear reinforcement ratio from 0.78 to 2.75, the gap between the DE FRP and steel contributions decreases, resulting in V_s/V_f values in the range from 0.22 to 0.53. The steel-to-FRP shear resistance ratio remains almost constant for steel-to-FRP shear reinforcement ratios higher than 2.75. This implies that the steel-to-FRP shear reinforcement ratio should be designed to be well below 2.75 in order to maximise the DE FRP contribution.

6.3. Effect of Tension Reinforcement Ratio

The experimental results showed that tension reinforcement ratio influenced failure mode but not gain due to DE FRP bars (see Table 2). The effect of tension reinforcement ratio on failure mode was further investigated by modelling DE FRP shear-strengthened beams nominally identical to the tested beams but with tension reinforcement ratios in the range from 0.45 to 4.15%, obtained by changing the diameter of tension steel bars.

Fig. 9 shows that the variation of normalised moment capacity (i.e. moment at failure (M_u) divided by flexural capacity (M_f)) with tension reinforcement ratio is also bilinear. A normalised moment capacity of 1.00 denotes flexural failure whereas M_u/M_f values less than 1.00 denote shear failure. All strengthened beam models with a tension reinforcement ratio less than 2.0% failed in flexure. On the other hand, all strengthened beam models with a tension reinforcement ratio more than 2.0% failed in shear. This finding clarifies the effect of tension reinforcement ratio on failure mode of DE FRP shear-strengthened beams.

7. Evaluation of TR55 Design Model

TR55 [14] is currently the sole standard document covering design of DE FRP shear strengthening systems. TR55 ignores the concrete contribution and assumes that the total shear force capacity (V_t) is composed of the steel and DE FRP contributions, V_s and V_f, respectively.

$$V_t = V_s + V_f \qquad (3)$$

The steel contribution is given by:

$$V_s = 0.78\frac{A_{sw}}{s}df_y cot\theta \quad (4)$$

where d is the beam effective depth, f_y is the yield strength of the steel shear reinforcement and θ is the inclination angle of the concrete struts.

The DE FRP contribution is given by:

$$V_f = \frac{\varepsilon_{fse}E_{fd}A_f}{s_f}W_{eff} \quad (5)$$

where ε_{fse} is the effective strain in the DE FRP bars (taken as 0.004 mm/mm), E_{fd} is the design Young's modulus of the DE FRP bars (MPa) and W_{eff} is the effective width (mm) over which the DE FRP bars may act and given by:

$$W_{eff} = \left(h - 2l_{b,max}\right) \quad (6)$$

where h is the strengthened depth (mm) and $l_{b,max}$ is the maximum anchorage length (mm) beyond which no additional capacity gain can be achieved, given by:

$$l_{b,max} = \frac{\varepsilon_{fse}E_{fd}A_f}{(\pi * d_b * \frac{\tau_b}{\gamma_A})} \quad (7)$$

where d_b is the DE FRP bar diameter (mm), τ_b is the average bond stress (MPa) over the anchored length and can be taken as 15 MPa in the absence of test data and γ_A is a partial safety factor for the adhesive material.

TR55 suggests that the steel and DE FRP shear contributions should be evaluated concurrently as they are integral parts of the total shear force capacity. Table 4 compares the FE results ($V_{t,FE}$) and TR55 predictions ($V_{t,TR55}$) with the total experimental shear force capacity ($V_{t,Exp}$). All safety factors are set equal to 1.00 for the purpose of comparison. Both the FE results and TR55 predictions had comparable standard deviations values (0.08 and 0.05, respectively), indicating small scatter of the predictions. However, TR55 design model significantly underestimated the total shear force capacity with a mean predicted-to-experimental value of

0.42. As previously demonstrated, the FE model provided accurate predictions of the total shear force capacity with a mean predicted-to-experimental value of 1.04.

One reason for the conservative predictions of TR55 design model is that it takes the effective strain in the DE FRP bars as 0.004 mm/mm. However, the experimentally measured strain values in the DE FRP bars intersected by the main shear cracks ranged from 0.005 to 0.015 mm/mm. Another reason is that TR55 assumes a fixed value for average bond stress whereas Caro et al. [25] demonstrated that it depends on many variables (e.g. concrete strength, DE FRP bar diameter and elastic modulus, adhesive type and embedded length).

A further shortcoming of the TR55 design model is that it does not consider the effect of steel-to-FRP shear reinforcement ratio. Fig. 10 shows the variations of total shear force capacity, predicted by the FE and TR55 models, with steel-to-FRP shear reinforcement ratio. The FE model, which has been demonstrated to accurately represent the experimental results, predicted a 25.1% decrease in total shear force capacity (from 104.7 to 78.4 kN) with the increase in steel-to-FRP shear reinforcement ratio from 0.17 to 4.35. The decrease in total shear force capacity is caused by the reduction in DE FRP contribution with increasing steel-to-FRP shear reinforcement ratio (see *Effect of Steel-to-FRP Shear Reinforcement Ratio* section). On the other hand, TR55 predictions did not show clear sensitivity to steel-to-FRP shear reinforcement ratio.

8. Conclusions

This paper presents results of an experimental and FE investigation on the structural behaviour of RC T-beams strengthened in shear with embedded FRP bars. Moreover, it provides insights into the influence of longitudinal and transverse reinforcement ratios on the structural behaviour of the strengthened beams. Furthermore, it evaluates the accuracy of the Concrete Society's Technical Report 55 shear strengthening design model for embedded FRP reinforcement. Based on the experimental and numerical results, the following conclusions are drawn:

- The total shear force capacity as well as the DE FRP and concrete contributions to shear strength decreased with increasing steel-to-FRP shear reinforcement ratio. Thus, calculating the DE FRP shear resistance as the difference between the strengthened and unstrengthened shear force capacities can lead to erroneous results.
- DE FRP bars should be designed in such a way that the steel-to-FRP shear reinforcement ratio is less than 2.75 in order to exploit DE FRP shear strengthening systems.
- The tension reinforcement ratio had a clear effect on failure mode. Tested and modelled strengthened beams with a tension reinforcement ratio equal to or less than 2.0% failed in flexure whereas tested and modelled strengthened beams with higher tension reinforcement ratios failed in shear. However, the tension reinforcement ratio did not influence the gain due to FRP bars.
- The control and GFRP-strengthened beams had comparable cracked stiffness whereas the CFRP-strengthened beam had higher cracked stiffness, demonstrating the effectiveness of CFRP bars in controlling crack opening.
- TR55 design model did not consider the effect of steel-to-FRP shear reinforcement ratio and underestimated the total shear force capacity with a mean predicted-to-experimental ratio of 0.42. On the other hand, the proposed FE model had a mean predicted-to-experimental ratio of 1.04 and correctly captured the reduction in shear strength with increasing steel-to-FRP shear reinforcement ratio.

Acknowledgements

The financial support of UK-India Education and Research Initiative (UKIERI) through Grant UKIERI-UGC 2017-18/17 is gratefully acknowledged. The first author also acknowledges the financial support of the Ministry of National Education of Turkey.

References

[1] Dirar S, Lees JM, Morley CT. Precracked RC T-beams repaired in shear with prestressed CFRP straps. ACI Structural Journal 2013; 110(5): 855-866.

[2] Dirar S, Lees JM, Morley CT. Precracked RC T-beams repaired in shear with externally bonded CFRP sheets. ACI Structural Journal 2012; 109(2): 215-223.

[3] Rizzo A, De Lorenzis L. Behavior and capacity of RC beams strengthened in shear with NSM FRP reinforcement. Construction and Building Materials 2009; 23(4): 1555-1567.

[4] Valerio P, Ibell T. Shear strengthening of existing concrete bridges. Structures and Buildings 2003; 156(1): 75-84.

[5] Chaallal O, Mofidi A, Benmokrane B, Neale K. Embedded through-section FRP rod method for shear strengthening of RC beams: performance and comparison with existing techniques. ASCE Journal of Composites for Construction 2011; 15(3): 374-383.

[6] Valerio P, Ibell TJ, Darby A. Deep embedment of FRP for concrete shear strengthening. Structures and Buildings 2009; 162(5): 311-321.

[7] Breveglieri M, Aprile A, Barros JAO. Embedded through-section shear strengthening technique using steel and CFRP bars in RC beams of different percentage of existing stirrups. Composite Structures 2015; 126: 101-113.

[8] Mofidi A, Chaallal O, Benmokrane B, Neale K. Experimental tests and design model for RC beams strengthened in shear using the embedded through-section FRP method. ASCE Journal of Composites for Construction 2012; 16(5): 540-550.

[9] Qin S, Dirar S, Yang J, Chan AHC, Elshafie M. CFRP shear strengthening of reinforced-concrete T-beams with corroded shear links. ASCE Journal of Composites for Construction 2015; 19(5): 04014081, 10pp.

[10] Dirar S, Theofanous M. Large-scale reinforced concrete T-beams strengthened in shear with embedded GFRP bars. In: Proceedings of the 8th International Conference on Advanced Composites in Construction (ACIC 2017), Sheffield, 5-7 September 2017. p. 114-119.

[11] Raicic V, Ibell T, Darby A, Evernden M, Orr J. Effectiveness of the deep embedment (DE) technique for shear strengthening of reinforced concrete continuous Beams. In: Proceedings of the 8th International Conference on Advanced Composites in Construction (ACIC 2017), Sheffield, 5-7 September 2017. pp. 6.

[12] Rahman R, Dirar S, Jemaa Y, Theofanous M, Elshafie M. Experimental behavior and design of exterior reinforced concrete beam-column joints strengthened with embedded bars. ASCE Journal of Composites for Construction 2018; 22(6): 04018047, 15pp.

[13] Qapo M, Dirar S, Jemaa Y. Finite element parametric study of reinforced concrete beams shear-strengthened with embedded FRP bars. Composite Structures 2016; 149: 93-105.

[14] The Concrete Society. Technical report TR55: design guidance for strengthening concrete structures using fibre composite materials. Camberley: The Concrete Society; 2012.

[15] Sogut K, Dirar S, Theofanous M, Faramarzi A. Effect of existing steel-to-embedded FRP shear reinforcement ratio on the behaviour of reinforced concrete T-beams. In: Proceedings of the 9th International Symposium on Advanced Composites in Construction (ACIC 2019), Birmingham, 3-5 September 2019. p. 11-16.

[16] Vecchio FJ. Disturbed stress field model for reinforced concrete: formulation. ASCE Journal of Structural Engineering 2000; 126(9): 1070-1077.

[17] Vecchio FJ, Collins MP. The modified compression field theory for reinforced concrete elements subject to shear. ACI Journal 1986; 83(2): 219-231.

[18] Wong PS, Vecchio FJ, Trommels H. VecTor2 & FormWorks user's manual (second edition). Toronto: University of Toronto; 2013.

[19] Bažant ZP, Oh BH. Crack band theory for fracture of concrete. Matériaux et Constructions 1983; 16(3): 155-177.

[20] Dirar S, Lees JM, Morley CT. Phased nonlinear finite-element analysis of precracked RC T-beams repaired in shear with CFRP sheets. ASCE Journal of Composites for Construction 2013; 17(4): 476-487.

[21] Thorenfeldt E, Tomaszewicz A, Jensen JJ. Mechanical properties of high-strength concrete and applications in design. In: Proceedings of the Symposium on Utilization of High Strength Concrete, Stavanger, 15–18 June 1987. p. 149–159.

[22] Vecchio FJ, Collins MP. Compression response of cracked reinforced concrete. ASCE Journal of Structural Engineering 1993; 119(12): 3590-3610.

[23] CEB-FIB. CEB-FIP model code 1990. London: Thomas Telford Services Ltd; 1993.

[24] Bentz EC. Explaining the riddle of tension stiffening models for shear panel experiments. ASCE Journal of Structural Engineering 2005, 131(9): 1422–1425.

[25] Caro M, Jemaa Y, Dirar S, Quinn A. Bond performance of deep embedment FRP bars epoxy-bonded into concrete. Engineering Structures 2017; 147: 448-457.

List of Figures

Fig. 1. Cross-sections and elevation of tested beams (dimensions in millimetres)

Fig. 2. Spacing of steel and FRP shear reinforcement (dimensions in millimetres)

Fig. 3. Shear force-deflection curves

Fig. 4. Crack patterns at failure

Fig. 5. Components of shear resistance

Fig. 6. Experimental components of shear resistance vs. steel-to-FRP shear reinforcement ratio: (a) Concrete contribution, (b) FRP contribution

Fig. 7. Experimental and FE-predicted shear force-deflection curves

Fig. 8. Effect of steel-to-FRP shear reinforcement ratio

Fig. 9. Effect of tension reinforcement ratio

Fig. 10. Comparison between FE results and TR55 predictions

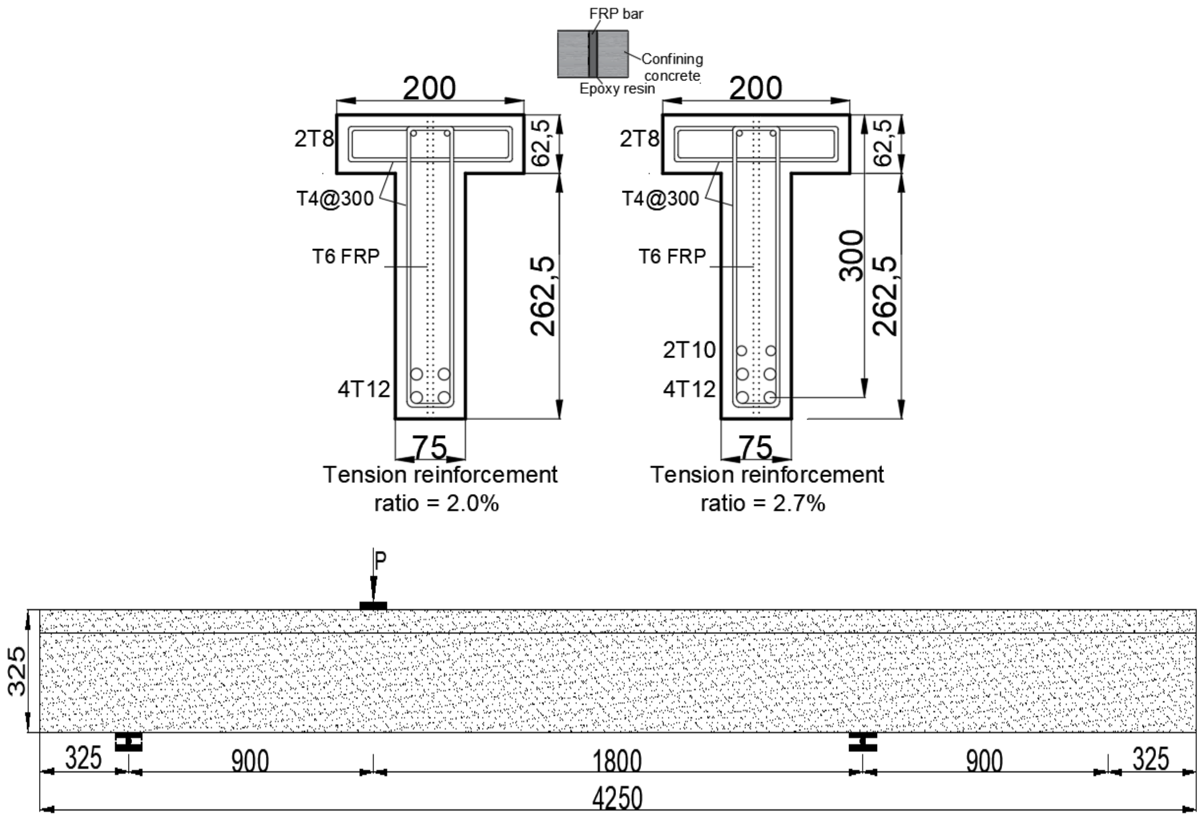

Fig. 1. Cross-sections and elevation of tested beams (dimensions in millimetres)

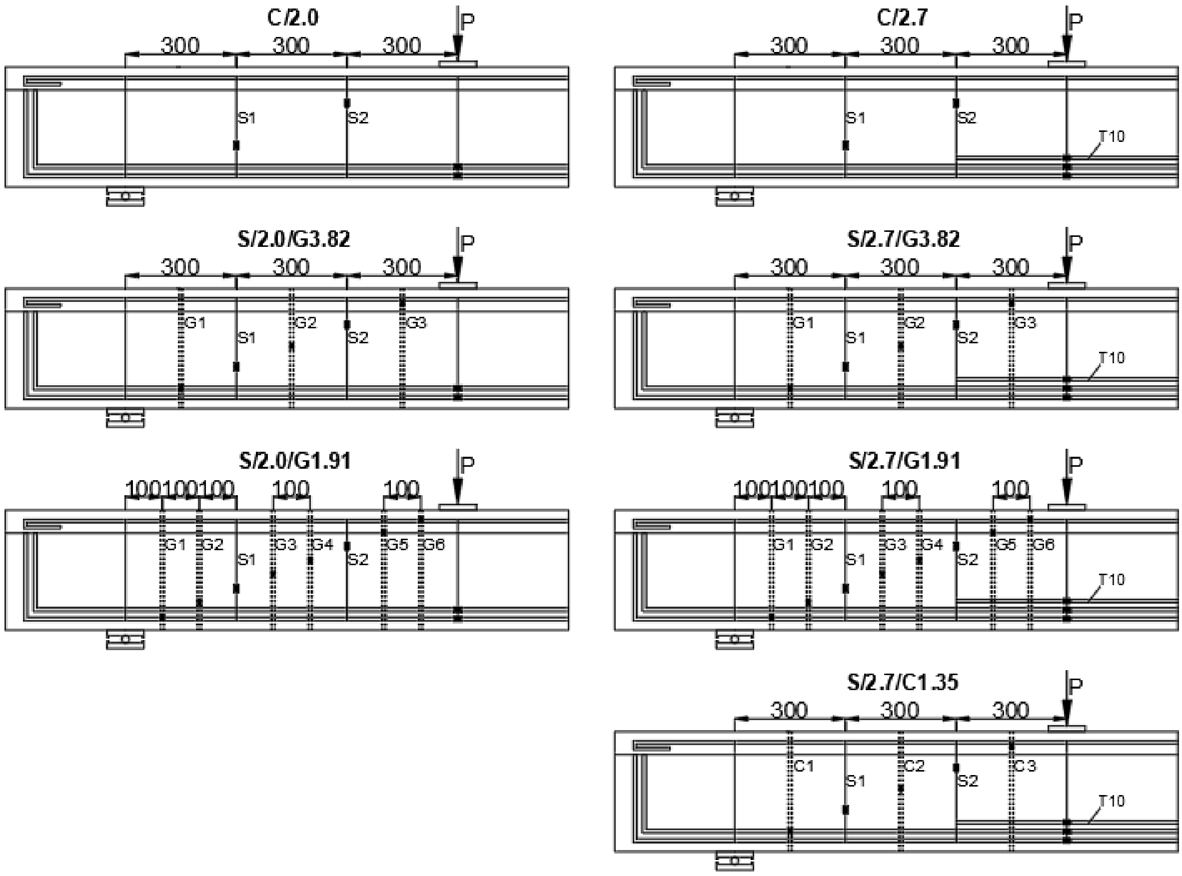

Fig. 2. Spacing of steel and FRP shear reinforcement (dimensions in millimetres)

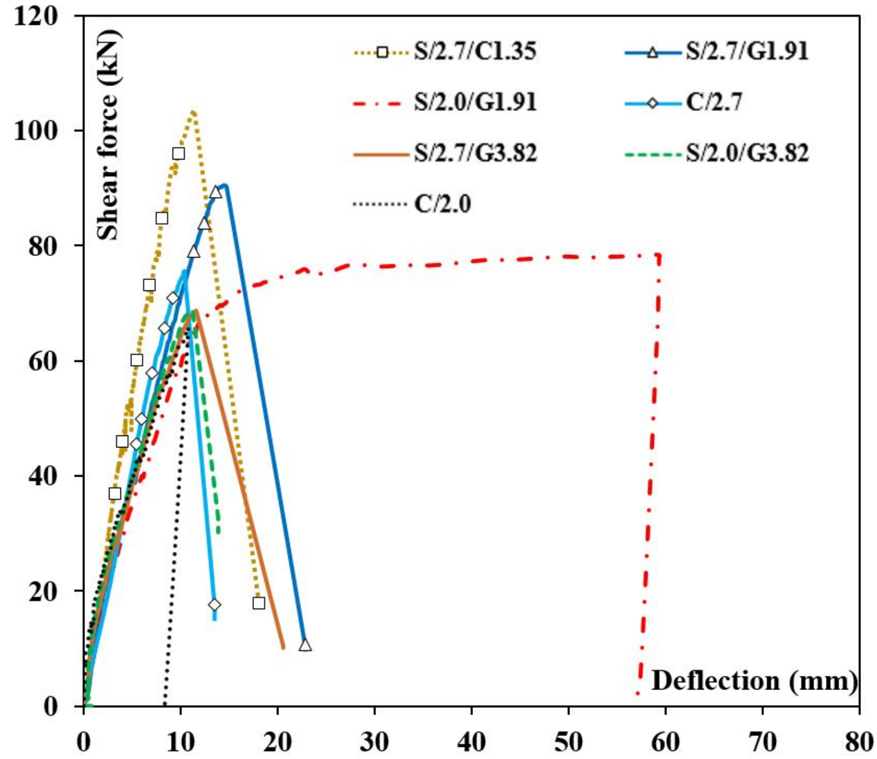

Fig. 3. Shear force-deflection curves


(C/2.0) (C/2.7)

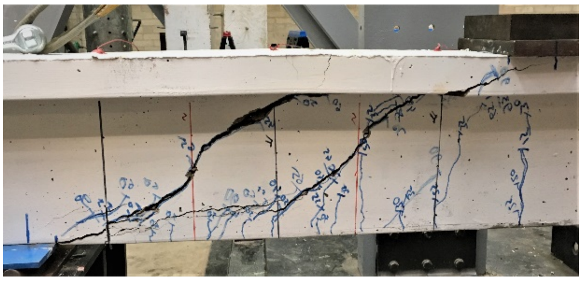


(S/2.0/G3.82) (S/2.7/G3.82)

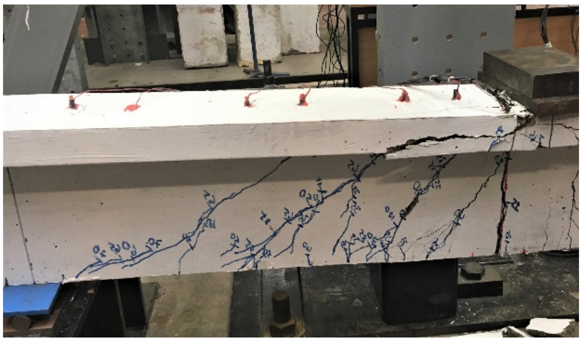
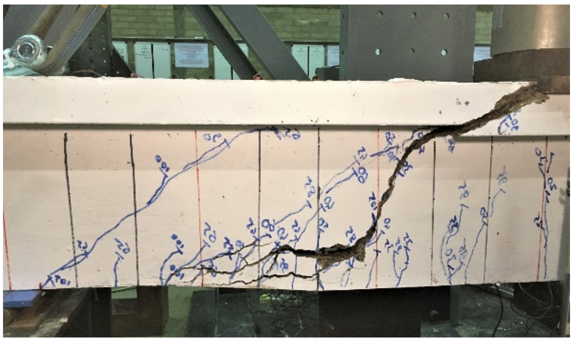

(S/2.0/G1.91) (S/2.7/G1.91)

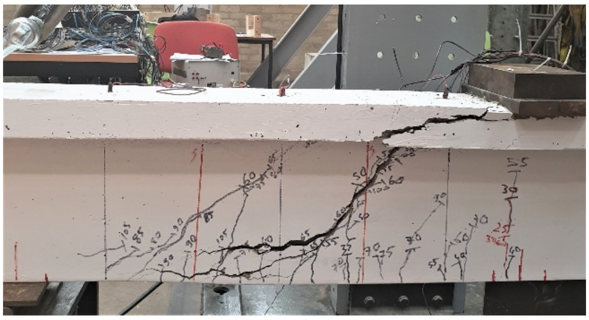

(S/2.7/C1.35)

Fig. 4. Crack patterns at failure

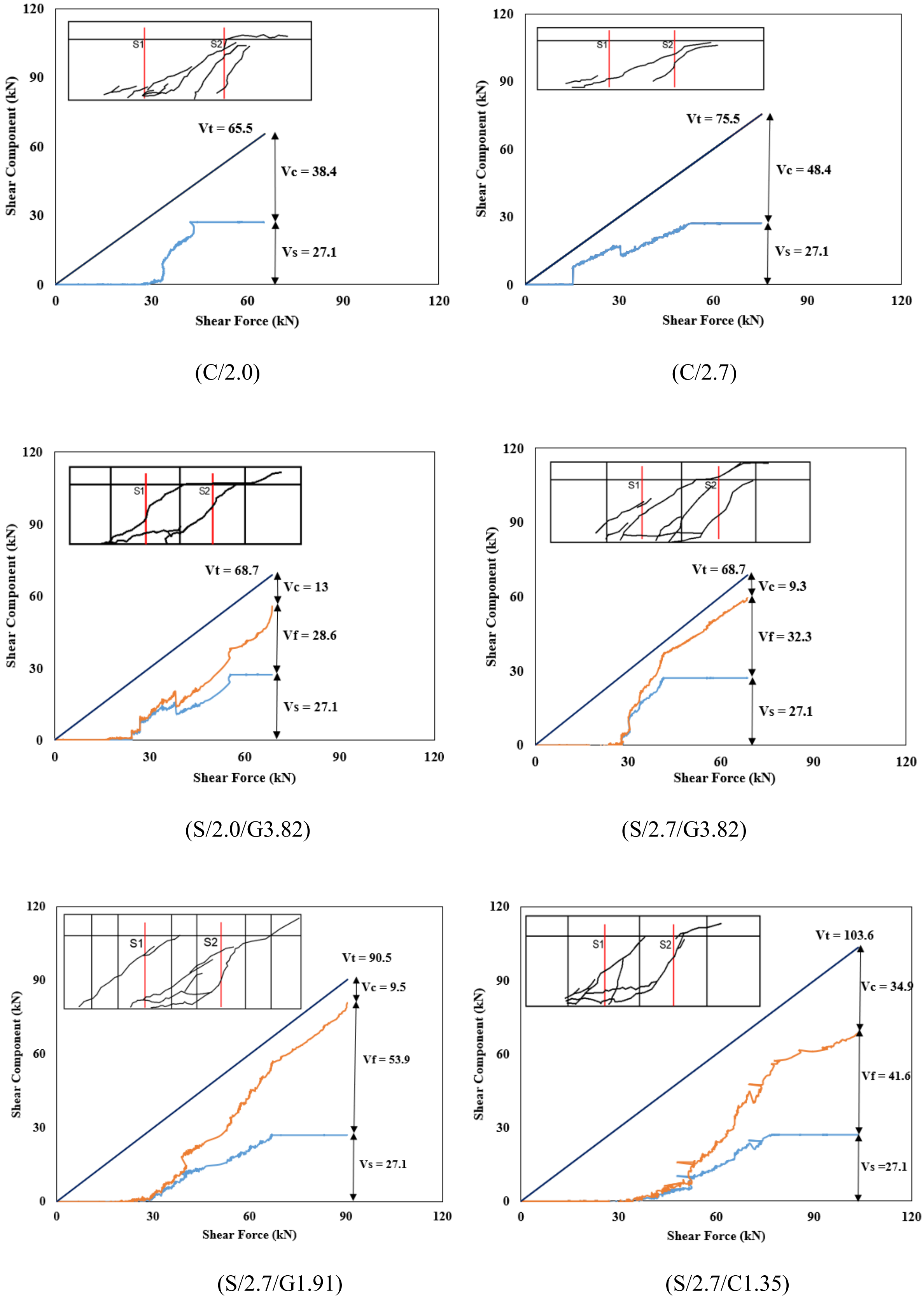

(C/2.0) (C/2.7)

(S/2.0/G3.82) (S/2.7/G3.82)

(S/2.7/G1.91) (S/2.7/C1.35)

Fig. 5. Components of shear resistance

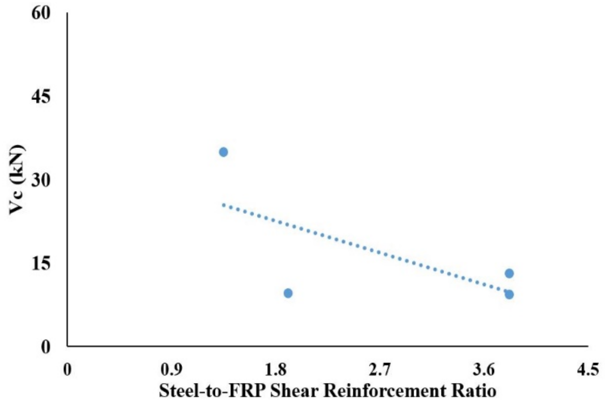

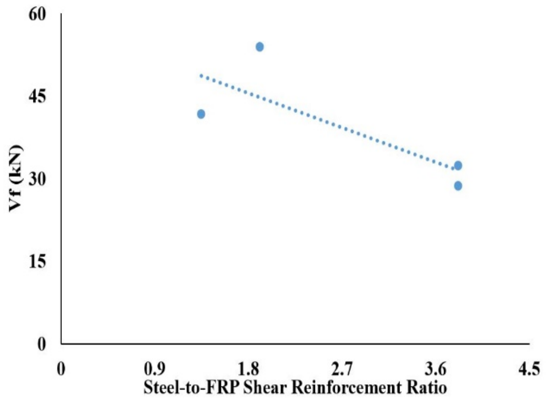

(a) (b)

Fig. 6. Experimental components of shear resistance vs. steel-to-FRP shear reinforcement ratio: (a) Concrete contribution, (b) FRP contribution

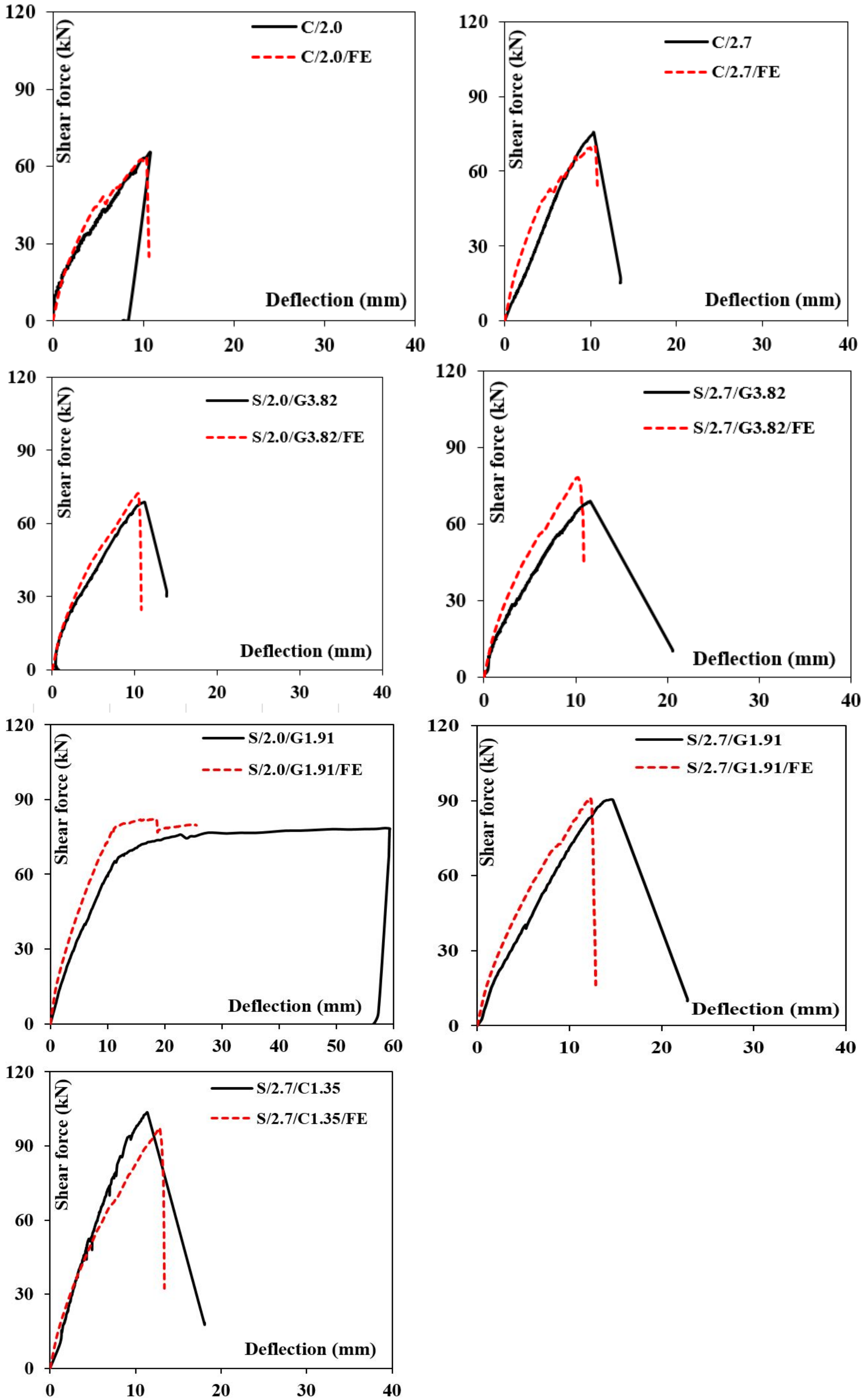

Fig. 7. Experimental and FE-predicted shear force-deflection curves

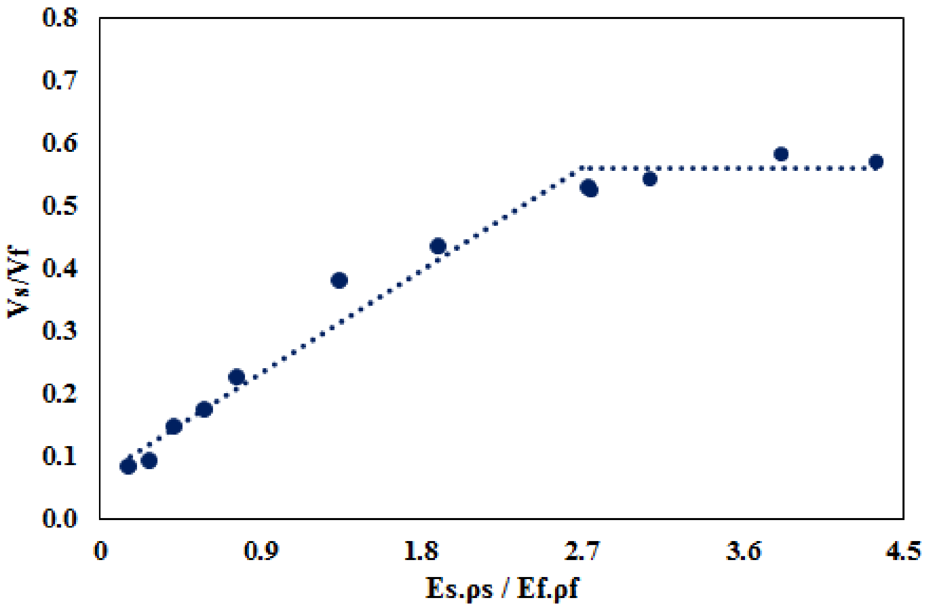

Fig. 8. Effect of steel-to-FRP shear reinforcement ratio

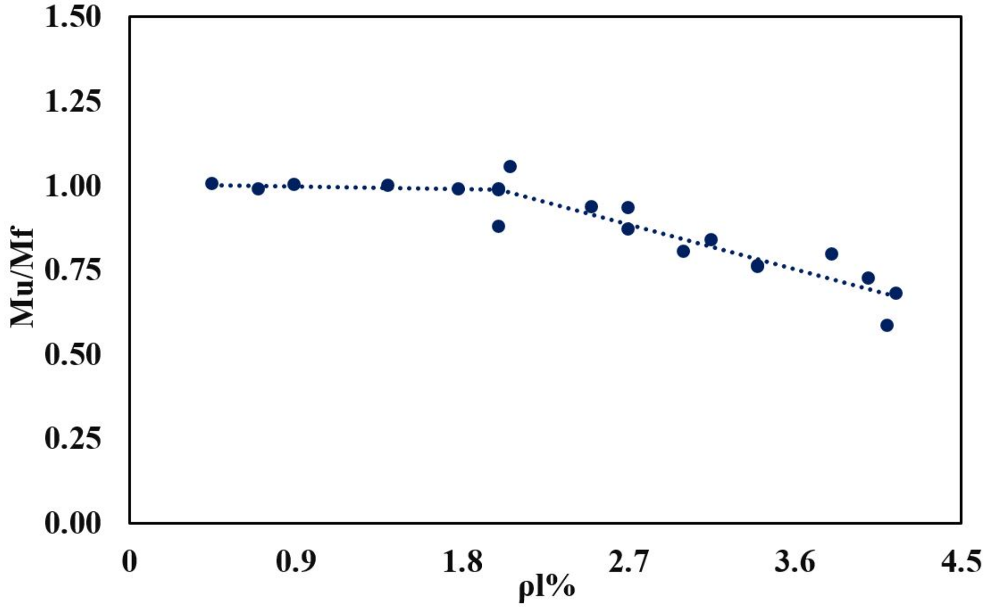

Fig. 9. Effect of tension reinforcement ratio

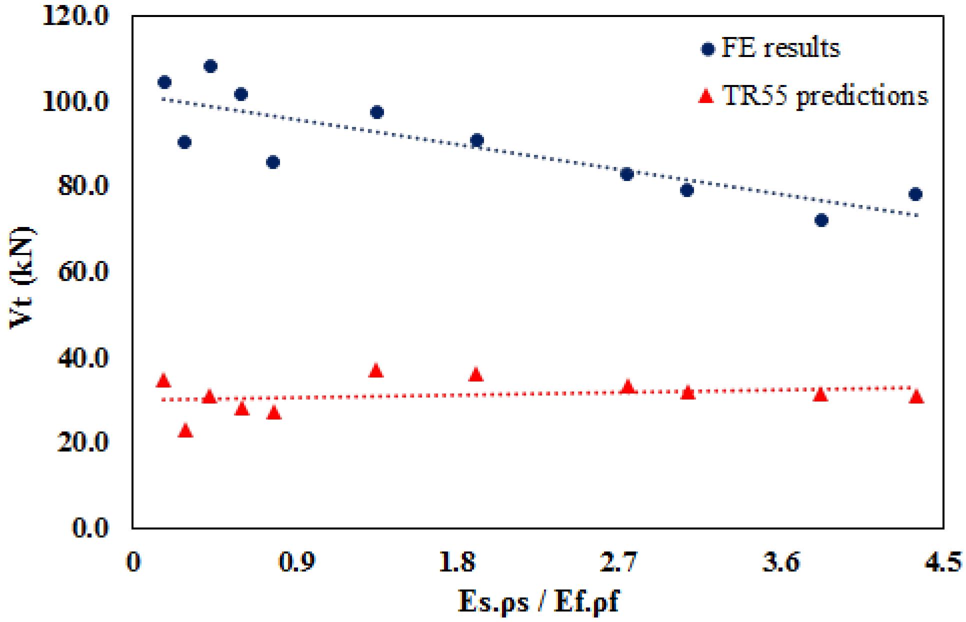

Fig. 10. Comparison between FE results and TR55 predictions

List of Tables

Table 1. Material properties

Table 2. Experimental results

Table 3. Comparison between experimental results and FE predictions

Table 4. Comparison between experimental, numerical and TR55 results

Table 1. Material properties

Property	Concrete	8, 10 and 12 mm steel bars	4 mm steel bars	6 mm sand-coated GFRP bars	6 mm sand-coated CFRP bars
Elastic Modulus (MPa)	-	200000	200000	46000	130000
Cylinder / cube Compressive Strength (MPa)	41 / 49	-	-	-	-
Ultimate Strain (mm/mm)	-	-	-	0.019	0.017
Yield Strength (MPa)	-	580	540	-	-
Ultimate Strength (MPa)	-	680	680	900	2300

Table 2. Experimental Results

Beam	Unstrengthened shear force capacity (kN)	Shear force at failure (kN)	Gain due to DE FRP bars (kN)	Gain due to DE FRP bars (%)	Failure mode
C/2.0	65.5	65.5	-	-	Shear
S/2.0/G3.82	65.5	68.7	3.2	4.8	Shear
S/2.0/G1.91	65.5	78.5	13	19.8	Flexure
C/2.7	75.5	75.5	-	-	Shear
S/2.7/G3.82	75.5	68.7	0	0	Shear
S/2.7/G1.91	75.5	90.5	15	19.8	Shear
S/2.7/C1.35	75.5	103.6	28.1	37.2	Shear

Table 3. Comparison between experimental results and FE predictions

Beam	Shear force at failure (kN)			Deflection at peak shear force (mm)		
	Experimental	FE Prediction	FE/Exp.	Experimental	FE Prediction	FE/Exp.
C/2.0	65.5	63.5	0.97	10.7	10.3	0.96
C/2.7	75.5	70.4	0.93	10.1	10.5	1.04
S/2.0/G3.82	68.7	72.2	1.05	11.2	10.4	0.93
S/2.7/G3.82	68.7	78.2	1.14	11.6	10.6	0.91
S/2.0/G1.91*	78.5	82.1	1.05	>50.0*	>25.0*	– *
S/2.7/G1.91	90.5	91.0	1.01	14.7	12.4	0.84
S/2.7/C1.35	103.6	97.4	0.94	11.3	12.6	1.12
Mean			1.01			0.97
Standard deviation			0.07			0.10

*Flexural failure

Table 4. Comparison between experimental, numerical and TR55 results

Beam	Total shear force capacity (kN)				
	$V_{t,Exp}$	$V_{t,FE}$	$V_{t,TR55}$	$V_{t,FE}$ / $V_{t,Exp}$	$V_{t,TR55}$ / $V_{t,Exp}$
S/2.0/G3.82	68.7	72.2	31.5	1.05	0.46
S/2.7/G3.82	68.7	78.2	31.5	1.14	0.46
S/2.7/G1.91	90.5	91.0	36.5	1.01	0.40
S/2.7/C1.35	103.6	97.4	37.3	0.94	0.36
Mean				1.04	0.42
Standard deviation				0.08	0.05